Mon. Not. R. Astron. Soc. **000**, 1–15 (2017) Printed 7 March 2024 (MN LATEX style file v2.2)

An infrared view of AGN feedback in a type-2 quasar: the case of the Teacup galaxy

C. Ramos Almeida[1,2⋆], J. Piqueras López[3,4,5], M. Villar-Martín[3,4], P. S. Bessiere[6]

[1] *Instituto de Astrofísica de Canarias, Calle Vía Láctea, s/n, E-38205, La Laguna, Tenerife, Spain*
[2] *Departamento de Astrofísica, Universidad de La Laguna, E-38206, La Laguna, Tenerife, Spain*
[3] *Centro de Astrobiología (INTA-CSIC), Carretera de Ajalvir, km 4, E-28850, Torrejón de Ardoz, Madrid, Spain*
[4] *Astro-UAM, UAM, Unidad Asociada CSIC, Facultad de Ciencias, Campus de Cantoblanco, E-28049, Madrid, Spain*
[5] *Department of Astrophysics, University of Oxford, Keble Road, Oxford OX1 3RH, UK*
[6] *Instituto de Astrofísica, Facultad de Física, Pontificia Universidad Católica de Chile, Casilla 306, Santiago 22, Chile*

ABSTRACT

We present near-infrared integral field spectroscopy data obtained with VLT/SINFONI of "the Teacup galaxy". The nuclear K-band (1.95–2.45 μm) spectrum of this radio-quiet type-2 quasar reveals a blueshifted broad component of FWHM∼1600-1800 km s^{-1} in the hydrogen recombination lines (Paα, Brδ, and Brγ) and also in the coronal line [Si VI]λ1.963 μm. Thus the data confirm the presence of the nuclear ionized outflow previously detected in the optical and reveal its coronal counterpart. Both the ionized and coronal nuclear outflows are resolved, with seeing-deconvolved full widths at half maximum of 1.1±0.1 and 0.9±0.1 kpc along PA∼72°–74°. This orientation is almost coincident with the radio axis (PA=77°), suggesting that the radio jet could have triggered the nuclear outflow. In the case of the H_2 lines we do not require a broad component to reproduce the profiles, but the narrow lines are blueshifted by ∼50 km s^{-1} on average from the galaxy systemic velocity. This could be an indication of the presence of a nuclear molecular outflow, although the bulk of the H_2 emission in the inner ∼2″ (∼3 kpc) of the galaxy follows a rotation pattern. We find evidence for kinematically disrupted gas (FWHM>250 km s^{-1}) at up to 5.6 kpc from the AGN, which can be naturally explained by the action of the outflow. The narrow component of [Si VI] is redshifted with respect to the systemic velocity, unlike any other emission line in the K-band spectrum. This indicates that the region where the coronal lines are produced is not co-spatial with the narrow line region.

Key words: galaxies: active – galaxies: nuclei – galaxies: evolution – galaxies: individual – galaxies: jets.

1 INTRODUCTION

Cosmological simulations require active galactic nuclei (AGN) feedback to regulate black hole and galaxy growth (Di Matteo et al. 2005; Croton et al. 2006). This process occurs when the intense radiation produced by the active nucleus sweeps out and/or heats the interstellar gas, quenching star formation and therefore producing a more realistic number of massive galaxies in the simulations (see Fabian 2012 for a review). Two major modes of AGN feedback are identified. Radio- or kinetic-mode feedback dominates in galaxy clusters and groups, where jet-driven radio bubbles heat the intra-cluster medium. This type of feedback is generally associated with powerful radio galaxies. Quasar- or radiative-mode feedback consists of AGN-driven winds of ionized, neutral, and molecular gas (Fabian 2012; Fiore et al. 2017). However, such a clear distinction between the two modes of feedback can be somewhat misleading. This is because it has been shown, through the detection of nuclear outflows, that radiative-mode feedback also acts in radio-galaxies (see e.g. Emonts et al. 2016 and references therein), whilst the presence of jets in quasars that are deemed to be radio-quiet can lead to faster and more turbulent AGN-driven winds (Mullaney et al. 2013; Zakamska & Greene 2014). Therefore, it is over-simplistic to consider the impact each mode of AGN-feedback has on its host galaxy in isolation.

One of the most efficient ways to identify the imprint of outflows in large AGN samples at any redshift is to search

⋆ Ramón y Cajal fellow. E-mail: cra@iac.es

for them in the warm ionized phase in the optical range (e.g. [O III]λ5007 Å). Indeed, during recent years it has become clear that ionized outflows are a ubiquitous phenomenon in type-2 quasars (QSO2s) at z$\lesssim$0.7 (Villar-Martín et al. 2011, 2014; Liu et al. 2013; Harrison et al. 2014; Karouzos et al. 2016). QSO2s are excellent laboratories to search for outflows and study their impact on their host galaxies, as the AGN continuum and the broad components of the permitted lines produced in the broad-line region (BLR) are obscured. Fast motions are often measured in QSO2s, with full-widths at half maximum (FWHM) >1000 km s^{-1} and typical velocity shifts (V$_s$) of hundreds km s^{-1}. These outflows are likely triggered by AGN-related processes and they originate in the high-density regions ($n_e \geqslant 10^3\ cm^{-3}$) within the central kiloparsecs of the galaxies. Optical integral field spectroscopy (IFS) studies have shown that these outflows can extend up to ∼15 kpc from the AGN (Humphrey et al. 2010; Liu et al. 2013; Harrison et al. 2014). However, these results have been recently questioned, as the reported outflow extents could be overestimated due to seeing smearing effects (Karouzos et al. 2016; Villar-Martín et al. 2016; Husemann et al. 2016).

Now that ionized outflows have been identified as a common process in QSO2, the next goal is to investigate their impact on other gaseous phases, such as the molecular and coronal phases. Since H_2 is the fuel required to form stars and feed the SMBH, the impact of the outflows in this gaseous phase is what might truly affect how systems evolve. Detecting coronal outflows is also interesting because, due to the high ionization potentials (IP$\gtrsim$100 eV; Mullaney et al. 2009; Rodríguez-Ardila et al. 2011; Landt et al. 2015) of these lines, they are unequivocally associated with nuclear activity. Coronal lines have intermediate widths between those of the broad and the narrow emission lines (FWHM∼500–1500 km s^{-1}) and are generally blueshifted and/or more asymmetric than lower-ionization lines (Penston et al. 1984; Appenzeller & Wagner 1991; Rodríguez-Ardila et al. 2011). This indicates that either coronal lines are produced in an intermediate region between the narrow-line region (NLR) and the BLR (Brotherton et al. 1994; Mullaney & Ward 2008; Denney 2012), and/or are related to outflows (Müller-Sánchez et al. 2006, 2011).

The near-infrared (NIR) range, and particularly the K-band, allows us to trace outflow signatures in the molecular, ionized and coronal phases simultaneously. In addition, because ionized outflows in QSO2 are heavily reddened (Villar-Martín et al. 2014), observing them in the NIR permits us to penetrate through the dust screen and trace the regions closer to the base of the outflow.

The rest-frame NIR spectrum of QSO2s at z<0.7 has not been fully characterised yet. To the best of our knowledge, this has been done for one QSO2 so far: Mrk 477 at z=0.037 (Villar Martín et al. 2015). Additionally, a NIR spectrum of the QSO2 SDSS J1131+1627 at z=0.173 was presented in Rose et al. (2011), but only Paα was detected. Here we explore the NIR spectrum of the QSO2 SDSS J143029.88+133912.0 (J1430+1339; at z=0.0852).

1.1 The Teacup galaxy

According to its [O III] luminosity ($5\times10^{42}\ erg\ s^{-1} = 10^{9.1} L_\odot$; Reyes et al. 2008), J1430+1339 is a luminous QSO2, and considering its position in the 1.4GHz–[O III] luminosity plane (Lal & Ho 2010) it is classified as radio-quiet ($L_{1.4GHz} = 5 \times 10^{23}\ WHz^{-1}$; Harrison et al. 2015, hereafter H2015). Nonetheless, it is a factor of 10 above the radio-FIR correlation found for star-forming galaxies (Villar-Martín et al. 2014; Harrison et al. 2014), which makes it a "radio excess source". The host galaxy shows clear signatures of a past interaction with another galaxy, in the form of shells, tails and chaotic dust lanes (Keel et al. 2015). J1430+1339 was nicknamed "the Teacup galaxy" because of the peculiar appearance of its extended emission-line region (EELR) in SDSS and HST images (Keel et al. 2012, 2015). This EELR is dominated by a filamentary bubble to the northeast (NE) with a radial extent of ∼12 kpc measured from the nucleus (see Figure 1). In the opposite direction there is another knotty emission-line structure resembling a fan extending up to ∼7 kpc. The Teacup has been proposed as a fading AGN candidate (Gagne et al. 2014).

The NE emission-line bubble coincides with the radio-continuum structure detected in VLA maps (H2015). These radio maps also show another radio bubble extending ∼10 kpc to the west, as well as two compact radio structures: a brighter one coincident with the AGN position, and a fainter one located ∼0.8 kpc northeast from the AGN (PA∼60°), identified by H2015 as high-resolution B (HR-B) region. According to the latter authors, this HR-B structure would be co-spatial with the base of the ionized nuclear outflow first reported by Villar-Martín et al. (2014) and Harrison et al. (2014) using the SDSS spectrum and IFU spectroscopy respectively. At the position of HR-B the outflow has an observed velocity of -740 km s^{-1} relative to the narrow component of [O III]λ5007 Å, which H2015 interpreted as gas accelerated by jets or quasar winds at that location. The latter authors also speculated that these jets/winds would be driving the 10–12 kpc radio bubbles.

Here we study the nuclear and extended NIR emission of the Teacup using seeing-limited SINFONI K-band data. In Section 2 we describe the observations and data reduction, in Section 3 we present the results on the nuclear and extended emission of the galaxy, and in Section 4 we discuss the observations and their implications. Throughout this paper we assume a cosmology with H_0=71 km s^{-1} Mpc^{-1}, Ω_m = 0.27, and Ω_Λ =0.73. At the redshift of the galaxy (z=0.0852), the spatial scale is 1.591 kpc arcsec^{-1}.

2 OBSERVATIONS AND DATA REDUCTION

We obtained K-band (1.95–2.45 μm) observations of the Teacup with SINFONI on the 8 m Very Large Telescope (VLT). The data were taken during the night of 2015 March 7th in service mode (Program ID: 094.B-0189(A)) with a total on-source time of 1800 s and at an airmass of 1.3–1.4. Due to the strong and rapid variation of the IR sky emission, the observations were split into short exposures of 300 s each, following a jittering O-S-S-O pattern for sky and on-source frames.

The observing conditions were clear and the seeing vari-

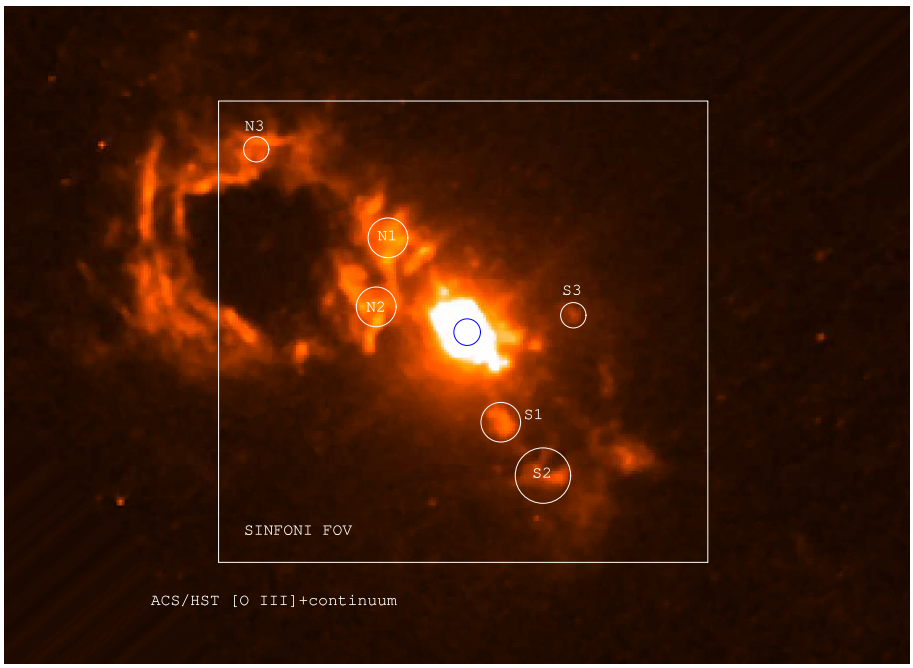

Figure 1. HST/ACS [O III]λ5007 Å image of the central 12.4″×17.2″ (19.7×27.4 kpc^2) of the Teacup. Note the smaller FOV covered by SINFONI (9.2″×8.7″$\simeq$ 14.6×13.8 kpc^2). The circles correspond to the different apertures chosen to extract the nuclear (blue central circle), eastern bubble (N1, N2, and N3), and western bubble NIR spectra (S1, S2, S3). North is up and east to the left.

ation over the on-source observing period was small according to the DIMM seeing monitor[1] (median optical seeing FWHM=1.05″, standard deviation=0.21″, and standard error=0.02″). To calculate the seeing FWHM in the K-band we used the photometric standard star observed immediately after the target, which appears slightly elongated along PA=88.3±0.1°, with a maximum FWHM=0.58″. Along the minor axis, the FWHM=0.46″. Therefore, the seeing error is dominated by the shape of the PSF rather than by the seeing variation during the observations. By averaging the maximum and minimum values of the FWHM measured for the star and by adding the seeing variation and PSF shape errors in quadrature, we get a seeing FWHM=0.52±0.06″ (∼830 pc resolution).

We used the 0.125″×0.250″ pixel^{-1} configuration, which yields a field-of-view (FOV) of 8″×8″ per single exposure. Due to the jittering process, the effective FOV in the case of our target is ∼9″×9″ (∼14×14 kpc^2). The spectral resolution in the K-band is R∼3300 (∼75 km s^{-1}) and the instrumental broadening, as measured from the OH sky lines, is 6.0±0.5 Å with a dispersion of 2.45 Å pixel^{-1}.

For the reduction of the data, we used the ESO pipeline ESOREX (version 3.8.3) and our own IDL routines for the telluric correction and flux calibration (see Piqueras López et al. 2012). We applied the usual calibration corrections of dark subtraction, flat fielding, detector linearity, geometrical distortion, wavelength calibration, and subtraction of the sky emission to the individual frames. The individual cubes from each exposures were then combined into a single data cube. To estimate the uncertainty in the wavelength calibration we used the atmospheric OH lines, from which we measured an error of 7.8 km s^{-1}.

The flux calibration was performed in two steps. First, to obtain the atmospheric transmission curves, we extracted the spectra of the standard stars with an aperture of 5σ of the best 2D Gaussian fit of a collapsed image. The spectra were then normalised by a blackbody profile of the appropiate T_{eff}, taking the most relevant absorption spectral features of the stars into account. The result is a sensitivity function that accounts for the atmospheric transmission. Second, we flux-calibrated the spectra of the stars using their 2MASS K-band magnitudes. Every individual cube was then divided by the sensitivity function and multiplied by the conversion factor to obtain a fully-calibrated data cube. The uncertainty in the flux calibration is ∼15%. We refer the reader to Piqueras López et al. (2012, 2016) for further details on the data reduction.

3 RESULTS

3.1 Nuclear spectrum

We extracted two K-band spectra of the nuclear region of the Teacup in two circular apertures of 0.5″ and 1.25″ diameter (∼0.8 and 2 kpc respectively), centred at the maximum of the Paα emission (see Section 3.1.1 for details). The minimum aperture was chosen to match the spatial resolution set by the seeing (FWHM=0.52±0.06″). In the following we will refer to the spectrum extracted in this aperture as the nuclear spectrum.

[1] http://archive.eso.org/wdb/wdb/asm/historical_ambient_paranal/query

3.1.1 Continuum shape

Figure 2 shows the observed nuclear spectrum of the Teacup with the emission lines labelled. We extracted the spectra centred at the peak of the ionized gas emission (as traced by Paα) because it does not coincide with the maximum of the K-band continuum emission. The peaks of the ionized gas and continuum emission are spatially offset by 0.125″ (∼200 pc; i.e. the size of one spaxel) with PA=0°. It is the case that 0.125″ is 1/4 the seeing size and thus we cannot resolve two spectra spatially offset by 0.125″.

The continuum slope rises towards the red, showing a maximum at ∼2.35 μm. The red dashed line in the left panel of Figure 2 corresponds to a blackbody of T=1200 K, which better reproduces the K-band nuclear continuum of the Teacup. This K-band spectral shape is not common in type-2 AGN, which generally show the opposite slope, but it has been reported for a few Seyfert 2 galaxies (e.g. NGC 7674 – Riffel et al. 2006; Mrk 348 – Ramos Almeida et al. 2009; NGC 4472 and NGC 7743 – Burtscher et al. 2015) and it has been interpreted as emission from AGN-heated nuclear dust near the sublimation temperature. In the case of the Teacup, considering the relatively large area probed by the nuclear spectrum (∼830 pc diameter), we are likely detecting hot polar dust within the ionization cones.

The change of the continuum slope with increasing aperture, as shown in the right panel of Figure 2 is also noteworthy. The red excess is only observed in the nuclear spectrum, it then flattens if we consider intermediate apertures and the slope becomes negative in the case of the large aperture spectrum (1.25″ diameter). The latter spectral shape resembles the typical K-band spectrum of Seyfert 2 galaxies (Riffel et al. 2006; Ramos Almeida et al. 2009; Burtscher et al. 2015). This change of slope with increasing aperture is due to the extra contribution from stellar light included in the larger apertures.

3.1.2 Emission line spectrum

By far the most prominent emission-line feature in the nuclear spectrum of the galaxy is Paα (see Figure 2), followed by Brδ, He Iλ2.060, Brγ, and the coronal line [Si VI]λ1.963 (all λ given in μm unless otherwise specified). We also detect several H_2 emission lines, indicative of the presence of a nuclear molecular gas reservoir. We fitted the nuclear emission-line spectrum with Gaussian profiles using the Starlink program DIPSO. Since the [Si VI] and H_2 1-0S(3) lines are blended (see central panel of Figure 3) we fixed the FWHM of H_2 1-0S(3) to match those of the other H_2 lines to enable us to obtain a reliable fit. In Table 1 we report the FWHMs corrected for instrumental broadening, velocity shifts (V_s) and fluxes resulting from our fits with DIPSO with their correspoding errors. The uncertainties in V_s include the wavelength calibration error (7.8 km s^{-1} as measured from the sky spectrum) and the individual fit uncertainties provided by DIPSO. In the case of the fluxes, the errors have been determined by adding quadratically the flux calibration error (15%) and the fit uncertainties.

We require two Gaussians to reproduce the hydrogen recombination lines and the [Si VI]λ1.963 line profiles. This includes a narrow component of FWHM∼400-460 km s^{-1} and a broad blueshifted component of FWHM∼1600–1800 km s^{-1}. We identify this broad component with the nuclear outflow reported from optical spectroscopy by Villar-Martín et al. (2014) and H2015. We discard the possibility of a BLR origin because the broad components are significantly blueshifted from the narrow component. Additionally not only are they detected in the permitted lines, but also in the [Si VI] coronal line.

Line	Nuclear spectrum FWHM (km s^{-1})	V_s (km s^{-1})	Line flux $\times10^{15}$ (ergs cm^{-2} s^{-1})
Paα	434±7	0±8	5.96±0.90
Paα (b)	1794±93	-234±35	3.64±0.56
Brδ	400±23	-5±11	0.30±0.05
Brδ (b)	1620±164	-361±109	0.23±0.05
Brγ	406±59	2±15	0.52±0.12
Brγ (b)	1807±1162	-133±209	0.32±0.12
He I	416±24	1±12	0.27±0.04
[*Si VI*]	463±22	54±11	0.47±0.08
[*Si VI*] (b)	1594±124	-77±55	0.67±0.11
H_2 1-0S(5)	401±114	-63±37	0.22±0.06
H_2 1-0S(3)	460	-89±14	0.28±0.05
H_2 1-0S(2)	452±52	-38±23	0.13±0.02
H_2 1-0S(1)	477±33	-14±17	0.32±0.05
H_2 1-0S(0)	...	...	:0.06
H_2 2-1S(1)	...	...	:0.06

Table 1. Emission lines detected in the nuclear spectrum of the Teacup (0.5″ diameter). FWHMs are corrected from instrumental broadening, and the velocity shifts (V_s) have been calculated relative to the central λ of the narrow component of Paα. In the case of the molecular lines 1-0S(0) and 2-1S(1), the reported fluxes correspond to upper limits at 3σ. The FWHM of the H_2 1-0S(3) line was fixed to obtain a reliable fit.

In Figure 3 we show the profiles and corresponding fits of the emission lines showing blueshifted broad components in the nuclear spectrum, namely Paα, Brδ, [Si VI], and Brγ. In the case of Paα we fitted a broad component of FWHM=1800±90 km s^{-1} with V_s=-234±35 km s^{-1} relative to the central wavelength of the narrow component (λ_c=20353.39±0.54 Å, giving z=0.08516±0.00003). For Brδ and Brγ we fitted blueshifted broad components consistent with that of Paα within the uncertainties (see Table 1).

The coronal line [Si VI] also shows a broad component of FWHM=1600±120 km s^{-1} blueshifted with respect to the narrow [Si VI] emission component. It is noteworthy that the narrow component is redshifted by V_s=54±11 km s^{-1} from the narrow Paα line, which is not observed in any other emission line in the K-band spectrum of the Teacup. As explained in Section 1, coronal lines are generally blueshifted and slightly broader than lower ionization emission lines (e.g. Rodríguez-Ardila et al. 2011). In the case of the Teacup, we detect the blueshifted broad component associated with the outflow, and a redshifted narrow component whose FWHM is the same as those of the recombination lines. This redshifted narrow component suggests that the coronal region and the region where the narrow core of the hydrogen lines is produced are different. Moreover, the lack of detection of coronal lines in the optical spectrum of the Teacup could be indicating that this coronal region is more reddened than the NLR. Using the SDSS spectrum

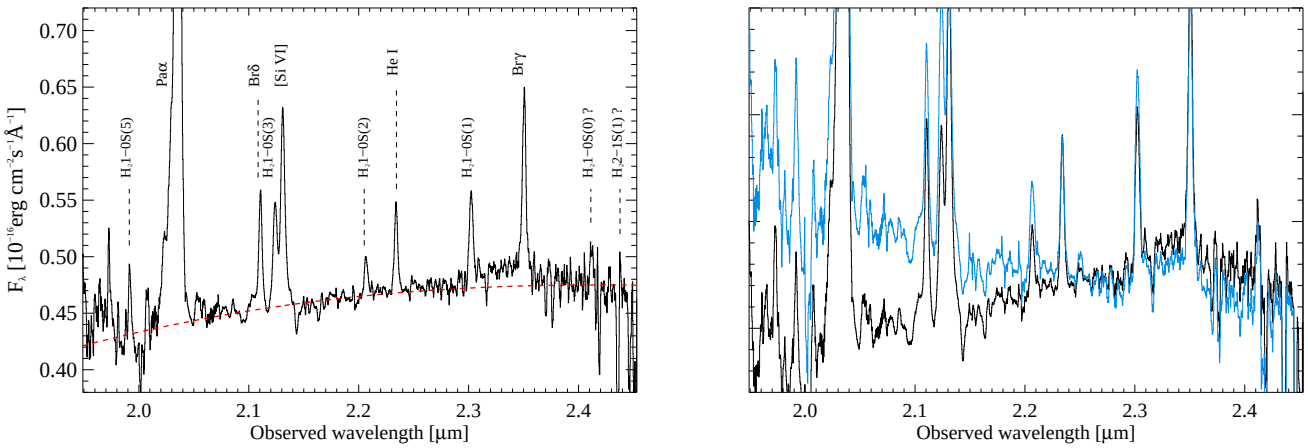

Figure 2. Left: Flux-calibrated nuclear spectrum of the Teacup, extracted in a circular aperture of 0.5″ diameter and smoothed using a 6 pixels boxcar. The most prominent emission lines are labelled. The molecular lines $H_2$1-0S(0) and 2-1S(1) are only marginally detected. The red dashed line corresponds to a blackbody of T=1200 K. Right: Spectra of the Teacup extracted in apertures of 0.5″ (black line) and 1.25″ diameter (blue line), normalized at 2.27 μm. Note the rise of the continuum at shorter wavelengths with increasing aperture.

presented in Villar-Martín et al. (2014) we measured [Fe VII]λ6087Å/[O I]λ6300Å=0.037±0.010, which is well below the range of ∼0.6-5.7 reported by Rodríguez-Ardila et al. (2006) for Seyfert galaxies with strong coronal lines detected in their NIR spectra.

Finally, in the case of the He Iλ2.060 and the molecular lines, single Gaussians with FWHM∼400–480 km s^{-1} were sufficient to reproduce the profiles (see Table 1). However, whilst neither the He I line nor the narrow core of the hydrogen recombination lines are shifted from the systemic velocity (as measured from the narrow component of Paα), all the H_2 lines are systematically blueshifted, with V_s=-51±32 km s^{-1} on average. This could be a first indication of a molecular outflow in the Teacup (see e.g. Müller-Sánchez et al. 2016 and references therein), although deeper observations are required to confirm it. It should also be noted that the use of the narrow component of Paα as a tracer of the systemic velocity is affected by uncertainties (Villar-Martín et al. 2014; Müller-Sánchez et al. 2016). Accurate measurements of the systemic velocity are needed to understand the kinematic behaviour of the H_2 lines.

3.1.3 *Emission line diagnostics*

To determine the degree of obscuration of the nuclear region of the Teacup we calculated the narrow and broad Paα/Brγ ratios in the two apertures considered here. By comparing them (see Table 2) with the theoretical value of 12.2 (Hummer & Storey 1987) we can determine the optical and infrared extinction (A_V and A_K respectively) by using the parametrization $A_\lambda \propto \lambda^{-1.75}$ (Draine 1989). For the narrow component, we measure a maximum value of A_V=2.8±1.4 mag in the nucleus of the Teacup (∼830 pc diameter). In the large aperture (∼2 kpc diameter) the level of obscuration decreases to 0.55±1.14 mag.

Following the same procedure, from the ratio of the broad components we measure A_V=3.5±1.9 mag in the nucleus of the Teacup and A_V=1.5±1.7 mag in the large aperture. The latter value of the extinction is consistent with A_V=1.9±0.3 mag reported by Villar-Martín et al. (2014) for the nuclear outflow as measured from the SDSS spectrum.

	Nuclear spectrum	Aperture 1.25″
Paα^n/Brγ^n	11.42±0.39	12.04±0.33
A_V^n (mag)	2.77±1.39	0.55±1.14
A_K^n (mag)	0.24±0.12	0.05±0.10
Paα^b/Brγ^b	11.23±0.52	11.76±0.50
A_V^b (mag)	3.46±1.90	1.54±1.73
A_K^b (mag)	0.31±0.17	0.14±0.15
$H_2$1-0S(1)/Brγ^n	0.61±0.40	0.94±0.34
M_{H_2} ($10^3 M_\odot$)	3.03±0.83	10.3±2.5
M_{cold} ($10^9 M_\odot$)	2.18±0.59	7.39±1.84

Table 2. Emission-line ratios and derived properties measured from the narrow and broad components of the lines in the spectra extracted in the two apertures considered here (0.5″ and 1.25″ diameter, or equivalently ∼0.8 and 2 kpc).

The ratio $H_2$1-0S(1)/Brγ can be used to disentangle the dominant excitation mechanism of the gas (see Table 2). In the two apertures considered we measure values in the range 0.6–0.9, consistent with AGN photoinization (this ratio is lower than 0.6 for starburst galaxies and higher for LINERs; Mazzalay et al. 2013). Although we observe a tendency in 1-0S(1)/Brγ to increase with the aperture, the values are consistent within the errors.

As can be seen from Figure 2, we detect several H_2 lines in the nuclear spectrum of the Teacup. In AGN, the lowest vibrational levels (v=1) of H_2 tend to be thermalized (i.e. excited by shocks and/or X-ray illumination; Hollenbach & McKee 1989; Maloney et al. 1996), while higher level transitions are populated due to non-thermal processes such as UV fluorescence (Black & van Dishoeck 1987). The 1-0S(1)/2-1S(1) line ratio is an excellent discriminator between thermal and non-thermal processes. It is $\leqslant$2 in gas excited by UV fluorescence and $\geqslant$5 in thermally-dominated gas (Mouri 1994). At the same time, the 1-0S(2)/1-0S(0) line ratio is sensitive to the strength of the

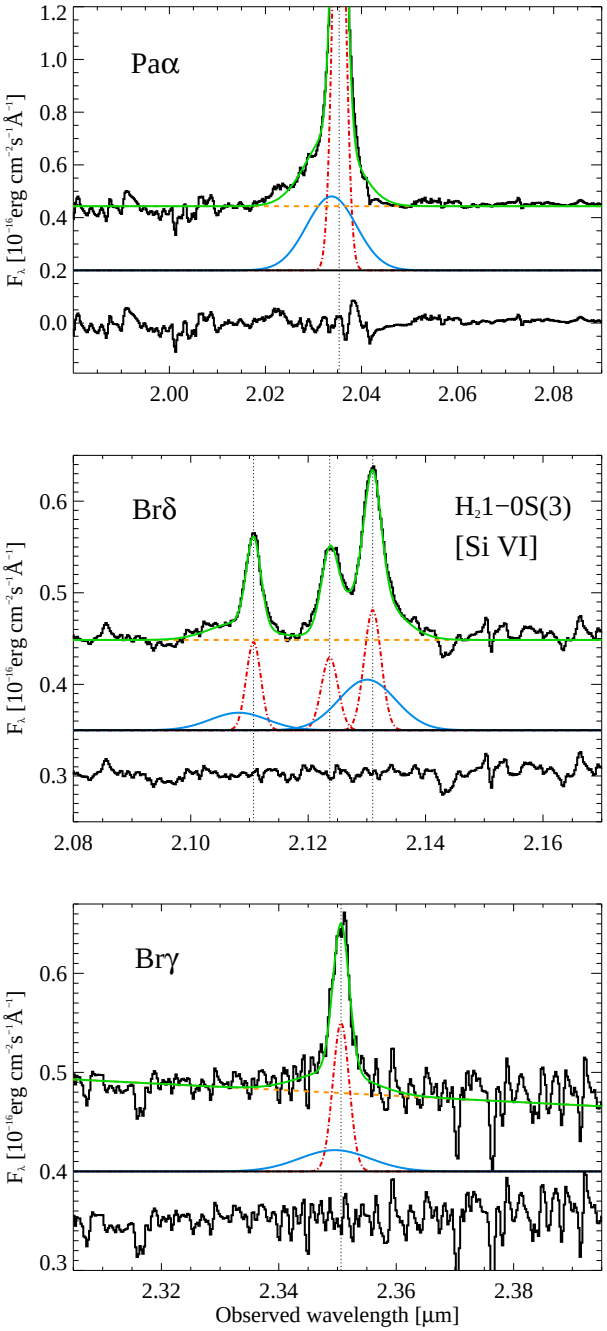

Figure 3. Line profiles showing a blueshifted broad component in the nuclear spectrum of the Teacup. Corresponding fits are shown as solid green lines. Solid blue and dot-dashed red Gaussians are the broad and narrow line components respectively, and the orange dashed line is the continuum. The Gaussians have been vertically shifted for displaying purposes. The insets at the bottom of each panel are the residuals, which in the case of the middle and bottom panels, have also been scaled vertically.

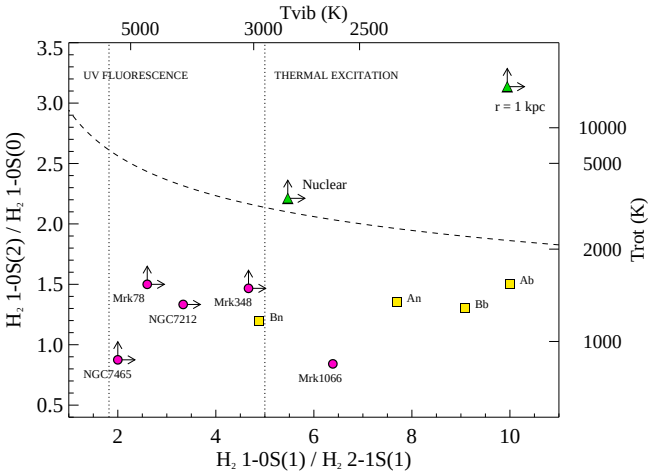

Figure 4. Molecular line ratios measured in the two apertures considered here (0.5″and 1.25″; green triangles). Pink circles are the ratios measured from the nuclear spectra of the Seyfert 2 galaxies studied in Ramos Almeida et al. (2009). Yellow squares correspond to the ratios derived for the broad and narrow components of regions A and B of the luminous IR galaxy (LIRG) and gas-rich merger NGC 3256 (Emonts et al. 2014). The dashed line indicates the locus of T_{vib}=T_{rot}. Vertical dotted lines delimitate the regions of "thermal" and "non-thermal" excitation from Mouri (1994).

incident radiation. In Figure 4 we show the line ratios that we have measured in the two apertures considered here. For comparison, we also plot the nuclear ratios of the five Seyfert 2 galaxies studied in Ramos Almeida et al. (2009) and those measured for the broad and narrow component of the lines in regions A and B of the gas-rich merger and luminous IR galaxy NGC 3256 (Emonts et al. 2014).

We find 1-0S(1)/2-1S(1) ratios $\geqslant$5, consistent with thermal excitation. Indeed, it can be seen from Figure 4 that the position of the Teacup ratios in the diagram is very different from those measured in Seyfert 2 galaxies. On the other hand, the lower limits on the 1-0S(1)/2-1S(1) line ratio are consistent with the values reported by Emonts et al. (2014) for regions A and B of the LIRG NGC 3256, but the 1-0S(2)/1-0S(0) values are significantly higher. This implies that although the molecular gas in the Teacup and in NGC 3256 is thermally excited, the strength of the incident radiation is not the same. This is expected considering that the presence of nuclear activity has not been confirmed yet in NGC 3256 (Emonts et al. 2014), while the Teacup hosts a very luminous AGN.

Using the two line ratios mentioned above we can derive the rotational and vibrational temperatures of the gas following Reunanen et al. (2002). Although we only have upper limits, in the case of the nuclear spectrum $T_{vib} \simeq T_{rot} \gtrsim$ 3000 K, which is characteristic of thermally excited gas. On the other hand, for the large aperture $T_{vib} << T_{rot}$, indicating that gas excitation is more complex than local thermal equilibrium (LTE) conditions ($T_{vib} = T_{rot}$).

Finally, we can use the $H_2$1-0S(1) luminosity to estimate the amount of molecular gas present in the nucleus of the Teacup. Following Mazzalay et al. (2013), the relation between the line flux and the warm molecular gas mass is

$$M_{H_2} \simeq 5.0875 \times 10^{13} (\frac{D}{Mpc})^2 (\frac{F_{1-0S(1)}}{erg\ s^{-1} cm^{-2}}) 10^{0.4 A_K}, \quad (1)$$

where D=387 Mpc and A_K is the extinction reported in Table 2. In the same Table we show M_{H_2} measured in the two apertures considered, as well as the masses of cold

molecular gas (M_{cold}) calculated by assuming a cold–to–warm mass ratio $M_{cold}/M_{H_2} \simeq 0.7 \times 10^6$. This ratio was derived observationally by Mazzalay et al. (2013) by comparing values of M_{cold} obtained from CO observations and H_2 luminosities for a large number of galaxies covering a wide range of luminosities, morphological types and nuclear activity. A similar ratio was reported by Dale et al. (2005) for a large sample of active and star-forming galaxies ($M_{cold}/M_{H_2} \simeq 10^{5-7}$).

In the nucleus of the Teacup we measure $M_{H_2} = (3.0 \pm 0.8) \times 10^3 M_\odot$ and $M_{cold} = (2.2 \pm 0.6) \times 10^9 M_\odot$. If instead of looking at the inner ∼830 pc of the Teacup we measure the molecular gas content in the inner 2 kpc, $M_{H_2} = (1.0\pm0.2)\times10^4 M_\odot$ and $M_{cold} = (7.4\pm1.8)\times10^9 M_\odot$. These cold gas masses are similar to those reported by Villar-Martín et al. (2013) for a sample of 10 QSO2s at z∼0.2–0.3 with CO measurements.

3.2 Ionized, coronal and molecular emission-line maps

In the previous sections we studied the spectra of the nuclear region of the Teacup. Here we take advantage of the spatial information provided by SINFONI and study the flux distribution and kinematics of Paα, [Si VI] and $H_2$1-0S(1). These three emission lines are the highest S/N representatives of the ionized, coronal and molecular phases of the gas respectively.

Paα is the only line that we detect in the extended emission-line structures (i.e. the NE bubble and the SW fan; see Section 3.2.2). We note, however, that the SINFONI FOV (9.2″×8.7″) does not cover the full extent of the NE bubble, as shown in Figure 1. In the case of the nuclear Paα and [Si VI] emission we needed two Gaussians to reproduce the observed line profiles and obtain corresponding flux, velocity and velocity dispersion (σ) maps. For the $H_2$1-0S(1) emission line (hereafter H_2) a single Gaussian was sufficient. Since the [Si VI] and $H_2$1-0S(3) lines are blended, we fixed the FWHM of the latter emission line to match that of $H_2$1-0S(1) and get reliable fits for the [Si VI]. In Figure 5 we show the flux, velocity and σ maps of the broad Paα, broad and narrow [Si VI] components, and H_2. These maps correspond to a 4″×4″ (6.4×6.4 kpc^2) FOV.

Using the flux maps we can estimate the projected sizes of each emission-line region. In Table 3 we show the observed and seeing-deconvolved FWHMs along the major axis in each case. We note that the intrinsic, deconvolved sizes for the central distribution of the emission lines considered here are approximate sizes. They have been obtained by applying the standard Gaussian deconvolution method based on the well-known quadrature relation $FWHM^2_{int} = FWHM^2_{obs} - FWHM^2_{seeing}$. All the emission-line maps shown in Figure 5 are resolved except the narrow [Si VI] maps.

The broad Paα and broad [Si VI] flux maps show similar morphologies, and are both elongated roughly in the same direction (PA∼72°–75°). We note that this elongation does not coincide with the orientation of the seeing major axis (PA=88.3±0.1°), as measured from the standard star. In the case of the broad [Si VI] flux map, two peaks are observed, separated by ∼0.3″ with a PA∼70° (although it is difficult to distinguish them in the [Si VI] flux map shown in Figure 5, they are evident when displayed in contours). One of these flux peaks coincides with the AGN position, as traced by the maximum of the Paα emission, and the other could be the coronal counterpart of the compact HR-B region detected by H2015 in the high-angular resolution VLA radio maps. The HR-B compact region is located 0.5″ northeast of the AGN position, with PA∼60°. As expected for outflow-related components, the maps of the broad Paα and broad [Si VI] emission are dominated by blueshifted velocity components, reaching maximum values of -250 km s^{-1}.

Line	FWHM (arcsec)	Seeing-decnv. FWHM (arcsec)	(kpc)	PA (deg)
Paα (b)	0.76±0.06	0.55±0.09	0.88±0.14	75.3±0.2
[*Si VI*] (b)	0.75±0.06	0.54±0.09	0.86±0.14	72.4±0.3
[*Si VI*] (n)	0.60±0.06	...	...	73.9±0.4
H_2 1-0S(1)	1.00±0.06	0.85±0.09	1.36±0.14	-7.7±0.5

Table 3. Radial sizes along the major axis and corresponding PAs of the broad Paα, broad and narrow [Si VI], and H_2 emitting regions as measured from the flux maps shown in Figure 5. Column 2 corresponds to observed FHWMs and columns 3 and 4 to seeing-deconvolved FWHMs.

The narrow [Si VI] emission-line maps (third row of Figure 5) are similar to those of the broad component, with the exception of the velocity map. The NE part of the emission is redshifted and the SW blueshifted, with maximum velocities of ±150 km s^{-1}. From the narrow [Si VI] flux map we can set constraints on the size of the coronal line region (CLR) of the Teacup. The observed FWHM that we measure is consistent with the seeing FWHM within the errors (see Table 3). Therefore the size of the CLR is formally unresolved and we can estimate an upper limit as $[(FWHM_{seeing}+3\sigma_{seeing})^2 - FWHM^2_{seeing}]^{0.5} = 0.47''\sim746$ pc.

The H_2 maps (bottom panels of Figure 5) are completely different to those of the ionized and coronal lines. They are elongated almost in the N–S direction (PA=-7.7±0.5°), which is roughly perpendicular to the orientation of the Paα and [Si VI] maps. The seeing-deconvolved FWHM along the major axis is 1.4±0.2 kpc (see Table 3). The global H_2 velocity field seems to be dominated by rotation, with maximum velocities of ±250 km s^{-1}. Deviations from this pattern are identified at some spatial locations, but they correspond to spaxels where the signal-to-noise is lower. The σ values are at a maximum in the central region (FWHM∼450 km s^{-1}) and decrease toward the edges (FWHM∼150 km s^{-1}).

3.2.1 Extent of the nuclear outflow

In Figure 6 we show Paα flux maps extracted in consecutive velocity intervals of 500 km s^{-1}, centred at the maximum of the line profile in the central spaxel (see Figure 7). These velocity cuts allow us to characterize the extent and orientation of the Paα emission in the core and the wings of the line.

In the central panel we see the Paα emission corresponding to the core of the line, which we have assumed as systemic redshift. From this map we can distinguish the nuclear emission (inner ∼2″) and the extent of the emission-line features covered by the SINFONI FOV (the NE bubble and the SW fan). The right and left middle panels correspond to the

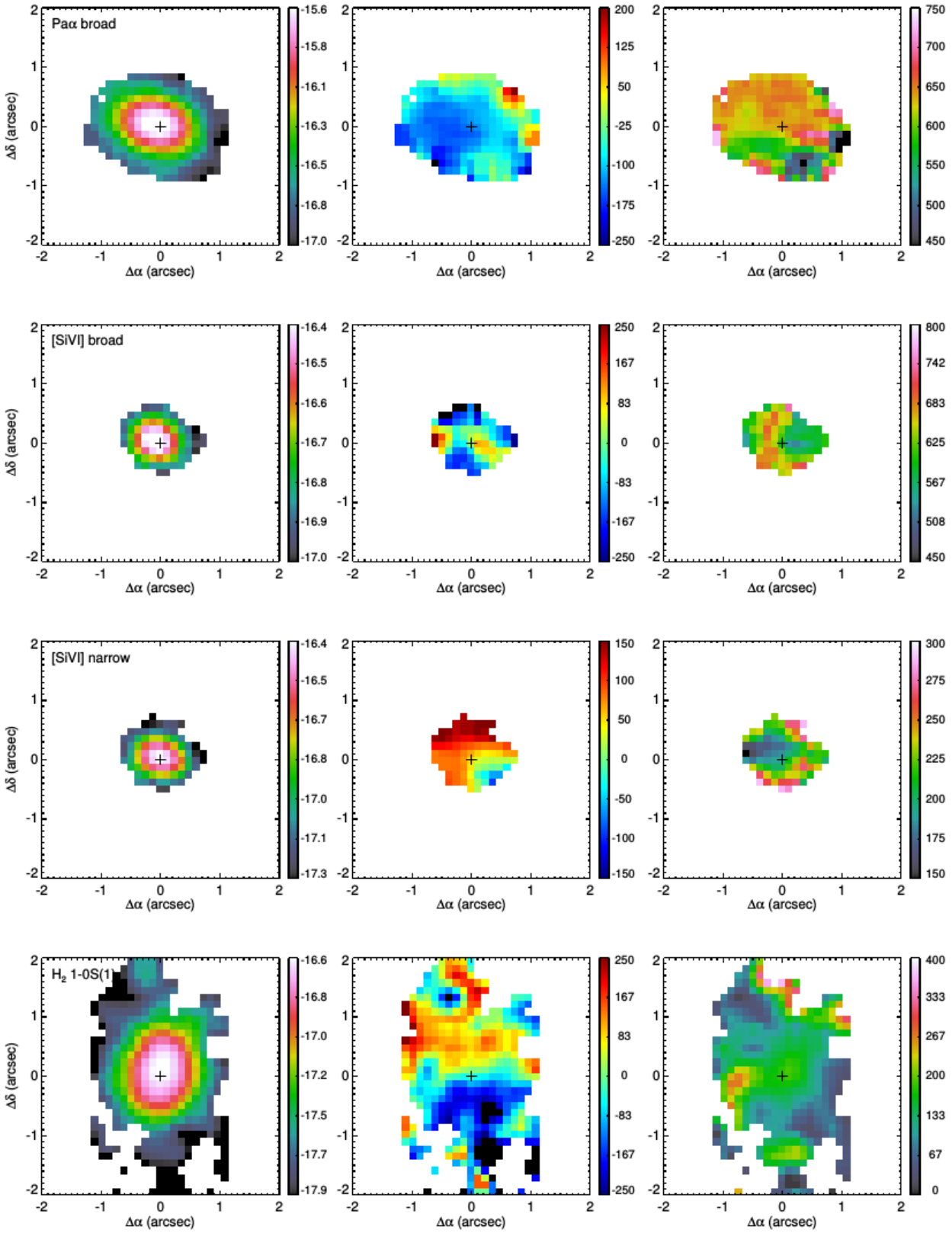

Figure 5. Flux, velocity and velocity dispersion maps of the broad Paα, broad and narrow [Si VI], and $H_2$1-0S(1) lines. The continuum-subtracted flux maps are in logaritmic scale and units are erg s^{-1} cm^{-2}. The velocity and dispersion maps are in km s^{-1}, and velocities are relative to the narrow core of Paα. The maps have been smoothed using a 2-spaxels boxcar. The brightest spaxel in the ionized gas emission is indicated with a cross. 1″ corresponds to 1.6 kpc. North is up and East to the left.

velocity bins centred at ±500 km s^{-1}, so the Paα wings dominate the emission. The nuclear emission appears elongated in the two panels and on larger scales, depending on whether we are sampling the blue or the red wing of Paα, we see the SW fan or the NE bubble, respectively.

The blueshifted broad component that we identified in the nuclear spectrum of the Teacup is sampled by the four negative velocity bins (see Figure 7). We fitted a Gaussian model to the nuclear region detected in the corresponding flux maps (middle left and top panels in Figure 6) and measured seeing-deconvolved FWHMs ranging from 1 to 1.1 kpc along the major axis, with PA=70°–75°. We measure a similar extension and orientation of the outflow when we sample the red wing of Paα (middle right and bottom left panels in Figure 6). This indicates that we can trace the nuclear outflow up to 1000 km s^{-1} beyond the core of Paα. It is noteworthy that the elongation of the nuclear Paα emission that we see at the highest velocities is less obvious at Δv=0 km s^{-1} (i.e. at the core of the line), confirming that the nuclear outflow is extended.

Therefore from the analysis of Figure 6 we conclude that the nuclear ionized outflow is resolved. The observed maximum extension, which corresponds to the -1000 km s^{-1} velocity bin, is FWHM=1.37±0.06″ along the 73.9±0.2° axis. As noted in Section 2, the standard star that was used to characterize the seeing is slightly elongated along PA=88.3±0.1°, with a maximum extension of 0.58″. Even considering the maximum value of the seeing, the nuclear ionized outflow is resolved, with a seeing-deconvolved FWHM=0.68±0.09″ (1.1±0.1 kpc).

We cannot repeat the same exercise for the [Si VI] emission line because its blue wing is blended with $H_2$1-0S(3) and it has lower signal-to-noise than Paα. However, if we fit a Gaussian component to the broad [Si VI] flux map shown in Figure 5, we measure a FWHM=0.75±0.06″, which corresponds to a seeing-deconvolved FWHM=0.54±0.09″ (0.9±0.1 kpc) along the major axis (PA=72.4±0.3°). Therefore, the coronal outflow is also resolved in the same direction as the ionized outflow.

3.2.2 Large-scale Paα emission

In Figure 8 we show the flux, velocity and dispersion maps of the narrow component of Paα in a 9.5″×9″ (15.1×14.3 kpc^2) FOV. The flux map resembles the morphology of the [O III] and Hα HST images (Keel et al. 2015). The bulk of the Paα emission is dominated by the nuclear component, and beyond we detect part of the NE bubble (radial size of ∼9.5 kpc), and the SW fan (∼7 kpc). The velocity map (central panel of Figure 8) is similar to the [O III] velocity map reported by H2015, although it reveals that the kinematics of the gas in the bubble and fan are different from those of the NLR. Whilst the central ∼2″ show a smooth velocity field, probably coincident with the rotation pattern of the galaxy, beyond this there is an abrupt change in velocity. The NE bubble is redshifted with maximum velocities of 300 km s^{-1} relative to systemic, and the SW fan is blueshifted with V_{max}=-300 km s^{-1}. The dispersion map also shows a practically constant line width within the central 2″ (FWHM∼450-500 km s^{-1}) and smaller values in the bubble and fan (FWHM∼200–300 km s^{-1}). We note that the FWHM>500 km s^{-1} (i.e. $\sigma \gtrsim 210$ km s^{-1}) that we measure around the nuclear region (∼1″ radius) corresponds to the transition zone where we no longer need to fit a broad component to reproduce the Paα profiles.

To study the properties of the extended Paα emission of the Teacup in more detail, we extracted spectra from different spatial locations in the bubble and fan. In Figure 1 we indicate the positions and apertures chosen for extracting the spectra in the galaxy nucleus, bubble (N1, N2, and N3) and fan (S1, S2, and S3). In Table 4 we report the different apertures chosen in each case and the radial distances from the nucleus. We show the six spectra extracted in the bubble and the fan in Figure 9. We used DIPSO to fit the emission lines using Gaussian profiles, and in Table 4 we report the corresponding FWHMs, V_s and line intesities. In the case of the bubble, single Gaussian components of FWHM∼300 km s^{-1} were sufficient to reproduce the narrow line profiles in the N1 and N2 spectra, extracted at ∼3 kpc from the nucleus. For the more distant N3 region (∼8 kpc from the nucleus) the FWHM is narrower (FWHM∼200 km s^{-1}). We note that, as we already knew from the Paα velocity map shown in Figure 8, these narrow Paα lines are significantly redshifted relative to the systemic velocity (V_s∼120–270 km s^{-1}; see Figure 9).

We also extracted three spectra mapping two bright regions within the fan (S1 and S2) and a bright knot at ∼3 kpc towards the west (S3). Two Gaussians were necessary to reproduce the narrow Paα profiles detected in the three spectra (see right panels of Figure 9). First, the blueshifted (V_s ∼-250 km s^{-1}) narrow components with FWHM=100–200 km s^{-1} already shown in the velocity map (see Figure 8). Second, in the case of the S1 and S3 spectra we required an additional component of FWHM∼200-300 km s^{-1} redshifted by V_s ∼40–120 km s^{-1} from systemic. For the S2 spectrum we fitted a slightly broader component of FWHM∼500 km s^{-1} whose V_s is consistent with that of the narrow component (V_s ∼-300 km s^{-1}).

Finally, we report tentative detection of a very broad Paα component of FWHM∼3000 km s^{-1} in five of the regions considered here (shown as blue Gaussians in Figure 9). These broad components are blueshifted relative to systemic in the bubble and fan, with V_s ranging between -60 and -310 km s^{-1}. Unfortunately, the combination of sky residuals and low signal–to–noise of the spectra prevents confirmation of these very broad Paα components. For this reason the results from the fits reported in Table 4 do not include the broad components.

4 DISCUSSION

4.1 The nuclear outflow

Based on the blueshifted broad lines detected in the nuclear K-band spectrum of the Teacup we confirm the presence of the nuclear ionized outflow previously reported by Villar-Martín et al. (2014) and H2015 using optical spectra, and we report the existence of its coronal counterpart. Although coronal outflows are commonly detected in Seyfert galaxies (e.g. Gelbord et al. 2009; Davies et al. 2014), this is one of the first detections of coronal outflows in QSO2s. Another example is Mrk 477, a QSO2 at z=0.037 with an [O III] luminosity of 3.3×10^{42} erg s^{-1} for which

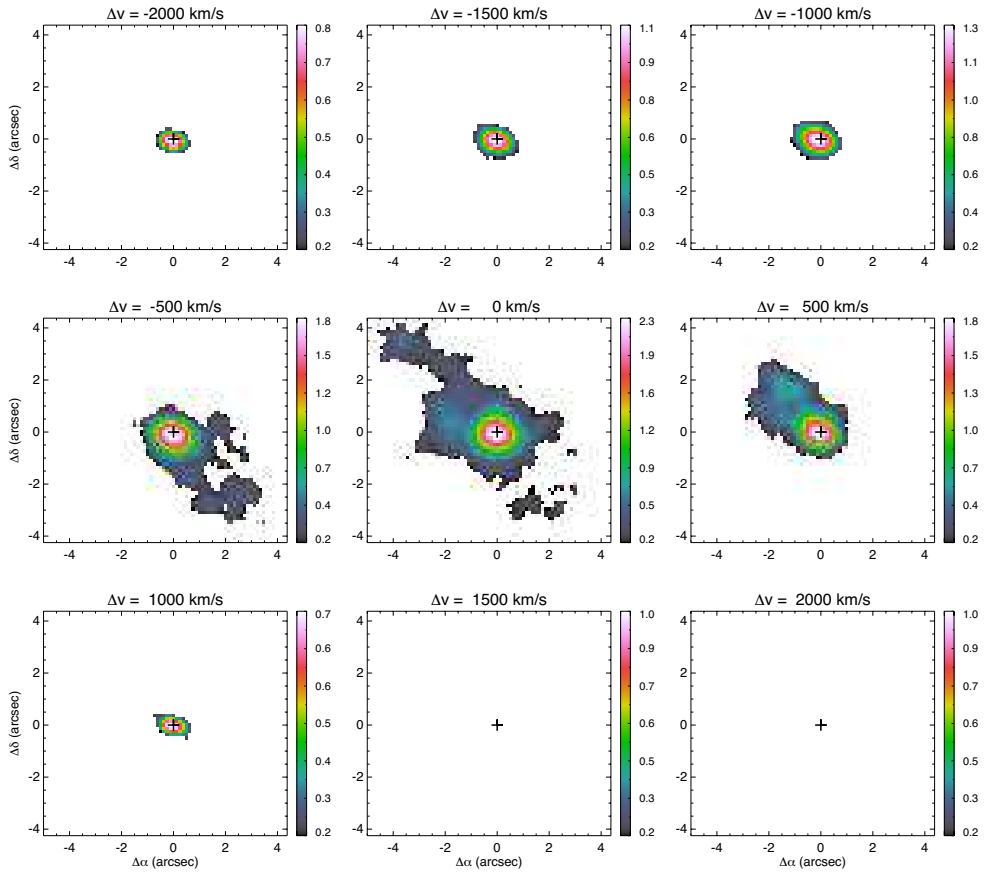

Figure 6. Continuum-subtracted Paα flux maps extracted in consecutive velocity intervals of 500 km s^{-1}, centred at the maximum of the line profile in the central spaxel (see Figure 7). The maps are in units of Log (σ) and have been smoothed using a 2-spaxels boxcar. North is up and East to the left.

Region	Distance to nucleus		Aperture diameter	Paα narrow component			Paα additional component		
	(arcsec)	(kpc)	(arcsec)	FWHM (km s^{-1})	V$_s$ (km s^{-1})	Flux × 10^{16} (ergs cm^{-2} s^{-1})	FWHM (km s^{-1})	V$_s$ (km s^{-1})	Flux × 10^{16} (ergs cm^{-2} s^{-1})
r2	0.0	0.0	0.50″	434±7	0±3	59.6±1.3	1794±93	-234±36	36.4±1.5
N1	2.1	3.4	0.75″	305±35	274±17	2.77±0.10	...	...	...
N2	1.7	2.8	0.75″	285±13	182±10	3.05±0.11	...	...	...
N3	5.1	8.1	0.50″	211±43	120±19	0.80±0.12	...	...	...
S1	1.8	2.9	0.75″	191±14	-263±10	1.68±0.10	307±116	116±42	0.40±0.12
S2	3.5	5.6	1.00″	93±28	-248±13	1.40±0.43	511±245	-300±41	1.62±0.35
S3	2.0	3.2	0.50″	205±41	-239±16	0.63±0.09	182±67	43±26	0.30±0.08

Table 4. Gaussian components fitted to the Paα emission line profiles detected in the nuclear spectrum and in the six apertures considered here. We note that these fits do not include the very broad components shown as blue Gaussians in Figure 9. FWHMs are corrected from instrumental broadening, and velocity shifts (V$_s$) are relative to the nuclear Paα narrow component.

Villar Martín et al. (2015) reported a blueshifted component of FWHM=2460±340 km s^{-1} in the high-ionization line [Fe VII]λ6087 Å (IP=99.1 eV).

The FWHM of this blueshifted component is larger than those measured in the optical for the central 3″ of the Teacup using the SDSS spectrum (FWHM∼1000 km s^{-1}; Villar-Martín et al. 2014) and GMOS/Gemini IFU data (maximum FWHM∼1000 km s^{-1}; Harrison et al. 2014). This is consistent with the outflow being reddened, as first claimed by Villar-Martín et al. (2014) and confirmed in this work, supporting the advantage of using NIR observations to trace AGN outflows closer to their origin.

We measure V$_s$=-234±35 km s^{-1} for the nuclear broad Paα component. This value is consistent with the velocities reported by Harrison et al. (2014) for the blueshifted component of the [O III] line measured from GMOS IFU data. They report a velocity offset of Δv=-150 km s^{-1} for the broad component in the galaxy-integrated spectrum, which corresponds to the central 5″×3.5″. However, if we look at the velocity maps (Figure A14 in Harrison et al. 2014), there

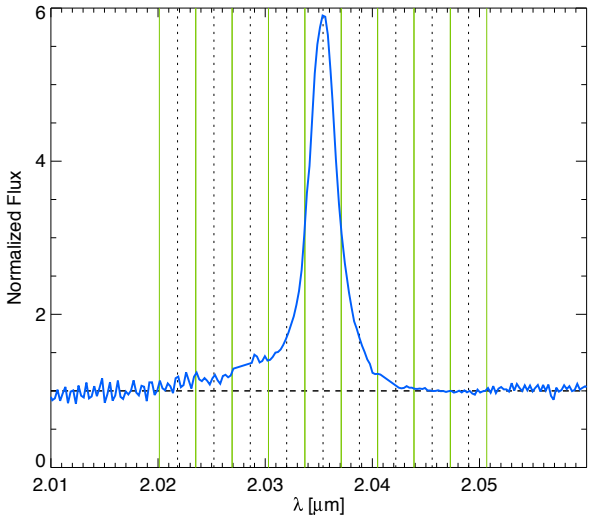

Figure 7. Paα line profile as extracted from the central spaxel. The continuum has been normalized (dashed line). The solid-green vertical lines indicate the velocity bins (from -2000 to 2000 km s^{-1} in steps of 500 km s^{-1}) used for extracting the nine flux maps shown in Figure 6.

is a strong velocity gradient around the position of the AGN, with a maximum velocity offset of -268 km s^{-1}. The broad Paα velocity map that we report here resembles the [O III] velocity field, showing maximum velocities of -250 km s^{-1}.

On the other hand, Villar-Martín et al. (2014) reported V$_s$=-70 km s^{-1} for the broad component of [O III] relative to the narrow core, but measured in an aperture of 3″ diameter ($\sim$5 kpc). The broad Paα maps, shown in the top middle panel of Figure 5, demonstrate that the SDSS fiber includes both blueshifted and redshifted components, which explains the smaller V$_s$ reported in Villar-Martín et al. (2014).

H2015 extracted a spectrum at the position of the HR-B region detected in the VLA radio maps and measured a FWHM=720 km s^{-1} with an observed velocity of -740 km s^{-1} relative to the narrow component of [O III]. Our SINFONI data have very high S/N in the nuclear region and yet, we do not require such a high velocity component to reproduce any of the profiles (see top middle panel of Figure 5). This could be due to the combined effect of reddening variation at different spatial locations, different aperture sizes and kinematic substructure within the outflow region.

Using the Paα and [Si VI] flux maps we confirm that both the ionized and coronal nuclear outflows are extended. We derived radial sizes of 1.1±0.1 kpc and 0.9±0.1 kpc respectively, with PA=72°–74°. This PA is almost identical to the radio jet orientation measured from the 1.4 GHz FIRST radio maps (PA$\sim$77°; Harrison et al. 2014). This could be indicating, as first suggested by H2015, that the interaction between the radio jet and the galaxy interstellar medium may have triggered and accelerated the nuclear outflow. The Teacup is then likely an example of radio jets driving outflows in a radio-quiet AGN. HST studies of Seyfert galaxies with linear radio structures showed strong evidence for interactions between the radio structures and the emission line gas in the NLR occurring on scales of $\lesssim$1 kpc (e.g. Axon et al. 1998). In QSO2s, the nuclear outflow in Mrk 477, which is thought to be triggered by the triple radio source present in this galaxy, has an estimated size of several hundreds of parsecs (Heckman et al. 1997; Villar Martín et al. 2015), and recent observations of different samples of luminous QSO2s at z<0.6, some of them with relatively high radio luminosities, reveal compact ionized outflow sizes of <1–2 kpc (Villar-Martín et al. 2016; Karouzos et al. 2016; Husemann et al. 2016). The case of powerful radio galaxies and quasars is different, with radio-induced outflows that can extend up to several kpc, even outside the galaxy boundaries (Tadhunter et al. 1994; Villar-Martín et al. 1999).

In the case of the H$_2$ lines we do not find evidence for broad components in the nuclear spectrum, and the velocity map shows a dominant rotation pattern. The only possible signatures of a molecular outflow in the Teacup are the nuclear narrow components blueshifted by -50 km s^{-1} on average relative to the systemic velocity. In any case, the bulk of the H$_2$ emission comes from the rotating gas distribution shown in Figure 5, and only a small percentage would be outflowing. Deeper observations and a more accurate determination of the systemic velocity of the galaxy are needed to confirm the presence of a nuclear molecular outflow.

The case of the Teacup is very different from that of its low-luminosity counterpart IC 5063. This Seyfert 2 galaxy has a similar redshift and radio-power as the Teacup but its NIR spectrum shows wings in the H$_2$ profiles as broad as those of the Brγ line. Furthermore, the H$_2$ emission shows a peak in brightness co-spatial with the radio lobe, which Tadhunter et al. (2014) interpreted as being due to gas cooling and forming molecules behind a jet-induced shock. The results presented here suggest a different scenario in the case of the Teacup, demonstrating that we do not always see broad molecular lines in the case of galaxies with strong jet-cloud interactions and ionized outflows.

This non-detection of broad H$_2$ components in the Teacup could be explained by a two-stage quasar wind scenario (Lapi et al. 2005; Menci et al. 2008; Zubovas & King 2012; Faucher-Giguére & Quataert 2012). Fast winds accelerated by the AGN interact with the galaxy ISM, reaching temperatures $\geqslant 10^7$ K. Once the gas cools down to $\sim 10^4$ K, it starts to emit warm ionized and coronal lines such as [O III], Paα, and [Si VI], but further cooling is necessary for the gas to emit in H$_2$.

4.2 Emission-line structures

The bulk of the Paα emission is dominated by the nuclear component, and beyond, the NE bubble and SW fan expand in opposite directions with projected velocities ±300 km s^{-1} (see Figure 8). This is entirely consistent with the [O III] velocity map reported by H2015 in a much larger FOV ($\sim$25″×25″).

We extracted spectra at different locations within the emission line structures and we found double-peaked Paα profiles in the SW fan with FWHMs=100–500 km s^{-1} which are indicative of disturbed kinematics. In contrast, in the NE bubble only one Gaussian is needed to reproduce the Paα lines, but we measure FWHMs=300 km s^{-1} at two different positions. For comparison, the extended non-outflowing ionized gas detected in the most dynamically disturbed mergers with nuclear activity show FWHM<250 km s^{-1} (Bellocchi et al. 2013). According to this comparison with merger dynamics, the detection of turbulent gas

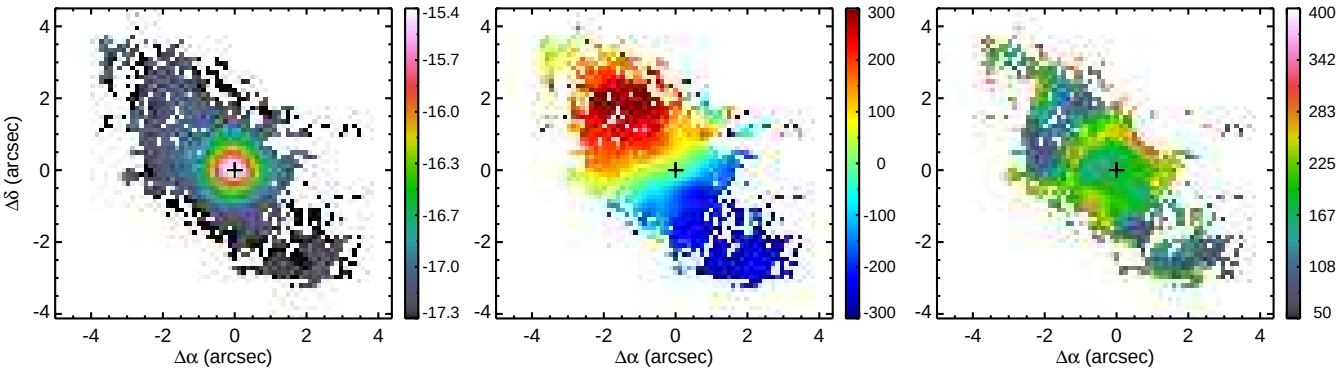

Figure 8. Same as in Figure 5 but for the narrow component of Paα and in a larger FOV of $9.5''\times9''$ (15.1×14.3 kpc^2).

in the Teacup is confirmed in apertures N1, N2, S1, and S2, located at distances between 2.8 and 5.6 kpc from the AGN, which correspond to ∼6.5 and ∼13.5 times half the seeing size.

Furthermore, in both the bubble and the fan we find tentative detection of a a very broad Paα component of FWHM∼3000 km s^{-1}. These broad components are blueshifted relative to systemic, with Vs ranging between -60 and -310 km s^{-1}. The velocity shifts that we measure for the very broad components and also for the narrow components (see Table 4) are consistent with those recently reported by Keel et al. (2017) using GMOS integral field spectroscopy. They claim that asymmetric [O III] profiles are present in different locations within the NE bubble, reaching maximum velocities of ±1000 km s^{-1}. Unfortunately, Keel et al. (2017) did not characterize the lines profiles quantitatively, so we do not know if they are detecting the very broad components that we see in our SINFONI data. Our interpretation is that, if these broad components are real, we would be detecting highly turbulent gas in a huge outflow that has cooled sufficiently to emit hydrogen recombination lines and be observable in the NIR. Nonetheless, independently of whether or not these broad components are real, the large scale gas (up to 5.6 kpc from the nucleus) shows turbulent kinematics that can be explained by the action of the outflow.

Finally, the H_2 maps presented here reveal a rotation pattern whose axis is misaligned with that of the narrow Paα emission, suggesting that the molecular gas is not coupled with the velocity distribution shown by the ionized gas. The rotating distribution of molecular gas detected in the Teacup could be the quasar-luminosity counterpart of the 100 pc-scale circumnuclear disks (CNDs) observed in nearby Seyfert galaxies using both NIR (Hicks et al. 2013) and sub-mm observations (García-Burillo et al. 2014). These CNDs rotate with similar velocities to those measured here ∼200–300 km s^{-1} (e.g. Helfer et al. 2003; García-Burillo et al. 2005). Furthermore they are not present in matched samples of quiescent galaxies (Hicks et al. 2013), indicating that they constitute a key element in the feeding of active SMBHs.

5 CONCLUSIONS

We have characterized the K-band emission-line spectrum of the radio-quiet QSO2 known as the Teacup galaxy. Thanks to the IFU capabilities of SINFONI we have not only studied the nuclear region of the galaxy, but also the Paα emission of its kpc-scale emission-line structures (i.e. the NE bubble and the SW fan) within a $\sim9''\times9''$ FOV. Our major conclusions are as follows:

- The nuclear K-band spectrum of the Teacup reveals the presence of a blueshifted component of FWHM∼1600–1800 km s^{-1} in the hydrogen recombination lines and also in the coronal line [Si VI]λ1.963. Therefore, we confirm the presence of the nuclear ionized outflow previously detected from optical spectra, and we reveal its coronal counterpart.
- The FWHM of the NIR lines associated with the nuclear ionized outflow are larger than those of their optical counterparts. This is consistent with the idea that, because of the lower extinction in the NIR, we can trace the outflow closer to its origin.
- Both the ionized and coronal nuclear outflows are spatially resolved, with seeing-deconvolved radial sizes of 1.1±0.1 and 0.9±0.1 kpc along the radio axis (PA=72°–74°). This suggests that the radio jet could have triggered the nuclear outflow.
- We find kinematically disrupted ionized gas (FWHM>250 km s^{-1}) at up to 5.6 kpc from the AGN, which can be naturally explained by the action of the outflow.
- The narrow component of [Si VI] is redshifted by V_s=54±11 km s^{-1} with respect to the systemic velocity, which is not the case for any other emission line in the K-band spectrum of the Teacup. This indicates that the coronal region is not co-spatial with the NLR.
- In the case of the H_2 lines, we do not require a broad component to reproduce the profiles seen in the nuclear spectrum, but the narrow lines are blueshifted by ∼50 km s^{-1} on average from the galaxy systemic velocity. This could be an indication of the presence of a molecular outflow, although additional observations are required to confirm this.
- The H_2 maps reveal a rotating structure oriented roughly perpendicular to the radio jet and the broad Paα and [Si VI] maps. This molecular gas structure could be the quasar-luminosity equivalent of the 100 pc-scale CNDs detected in Seyfert galaxies.
- We report tentative detection of very broad Paα components (FWHM∼3000 km s^{-1}) at different locations across the NE bubble and SW fan (at up to 5.6 kpc from the AGN).

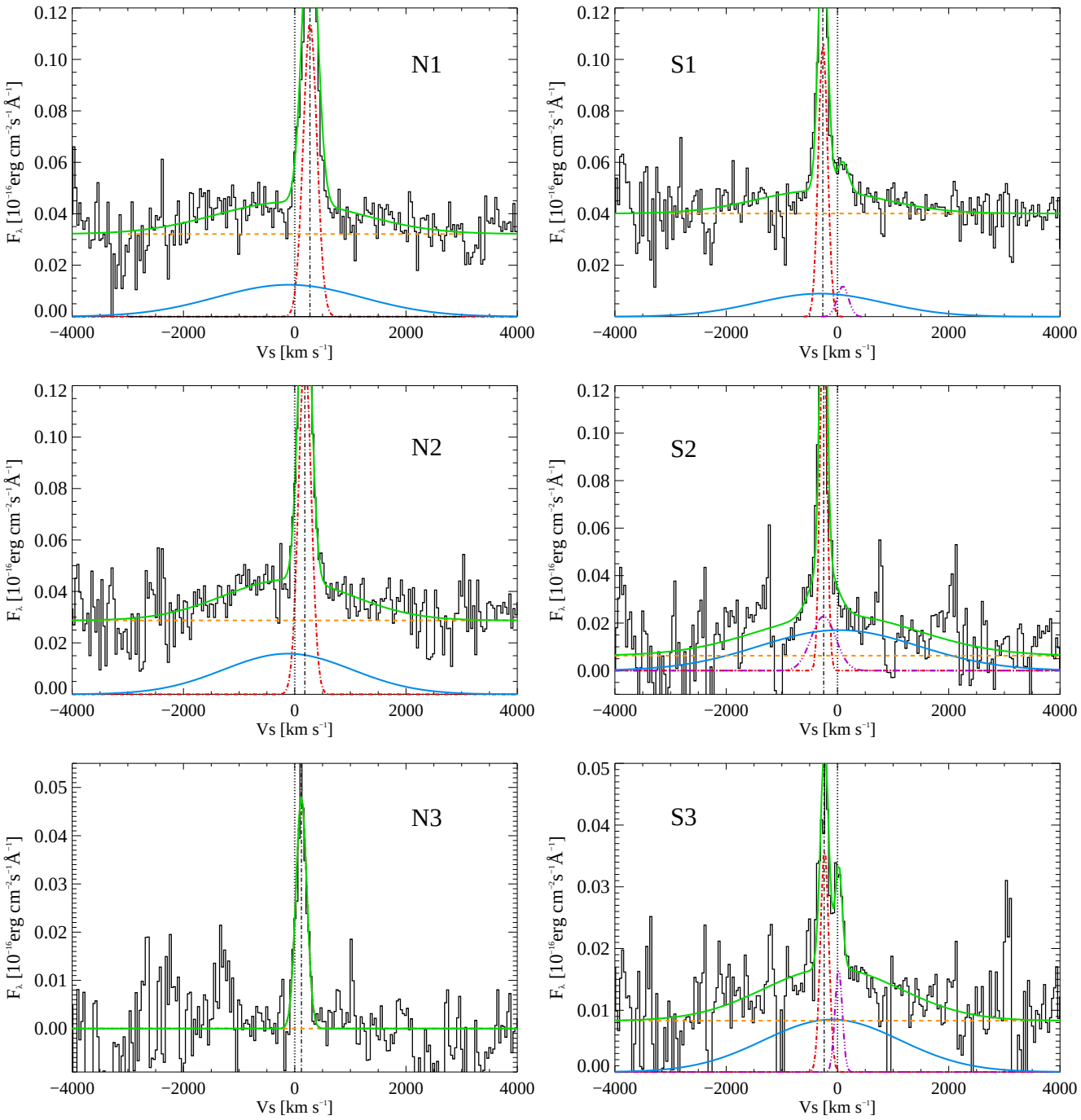

Figure 9. Paα line profiles detected at the different spatial locations indicated in Figure 1 and Table 4. N1, N2, and N3 spectra correspond to the NE bubble and S1, S2, and S3 to the SW fan. Corresponding fits and continua are shown as green solid and orange dashed lines. Dot-dashed red Gaussians correspond to the narrow Paα component and solid purple Gaussians to the additional Paα components described in Table 4. The very broad components tentatively detected in all the regions considered except N3 are shown as solid blue Gaussians. The vertical dotted line indicates zero velocity as set from the nuclear narrow component of Paα, and the dot-dashed line is V$_s$ measured for each line.

If confirmed, such extremely turbulent components could be hot shocked gas that has cooled sufficiently to be observable in Paα.

ACKNOWLEDGMENTS

Based on observations made with ESO Telescopes at the Paranal Observatory under programme ID 094.B-0189(A). First, we would like to acknowledge the constructive feedback and suggestions of the referee. CRA acknowledges the Ramón y Cajal Program of the Spanish Ministry of Econ-

omy and Competitiveness through project RYC-2014-15779 and the Spanish Plan Nacional de Astronomía y Astrofisíca under grant AYA2016-76682-C3-2-P. JPL acknowledges support from the Science and Technology Facilities Council (STFC) grant ST/N002717/1 and the Spanish Plan Nacional de Astronomía y Astrofisíca under grant AYA2012-39408-C02-01. MVM acknowledges support from the Spanish Ministerio de Economía y Competitividad through the grants AYA2012-32295 and AYA2015-64346-C2-2-P. PSB acknowledges support from FONDECYT through grant 3160374. The authors acknowledge the data analysis facilities provided by the Starlink Project, which is run by CCLRC on behalf of PPARC. We finally acknowledge José Antonio Acosta Pulido, Santiago García Burillo, Richard Davies, Erin Hicks, and Clive Tadhunter for useful comments that have substantially contributed to improve this work.

REFERENCES

Appenzeller, I., Wagner, S. J. 1991, A&A, 250, 57
Axon, D. J., Marconi, A., Capetti, A., Macchetto, F. D., Schreier, E., Robinson, A. 1998, ApJ, 496, L75
Bellocchi, E., Arribas, S., Colina, L., Miralles-Caballero, D. 2013, A&A, 557, 59 Cabrera-Lavers, A. 2017, MNRAS, 466, 3887
Black J. H., van Dishoeck E. F. 1987, ApJ, 322, 412
Brotherton, M. S., Wills, B. J., Francis, P. J., Steidel, C. C. 1994, ApJ, 430, 495
Burtscher, L., et al. 2015, A&A, 578, 47
Croton, D. J., et al. 2006, MNRAS, 365, 11
Dale, D. A., Sheth, K., Helou, G., Regan, M. W., Hüttemeister, S. 2005, AJ, 129, 2197
Davies, R. I., et al. 2014, ApJ, 792, 101
Denney, K. D. 2012, ApJ, 759, 44
Di Matteo, T., Springel, V., Hernquist, L. 2005, Nature, 433, 604
Draine, B. T. 1989, 22nd ESLAB Symp., Infrared Spectroscopy in Astronomy, ed. B. H. Kaldeich (ESA SP-290; Paris: ESA), 93
Emonts, B. H. C., Morganti, R., Villar-Martín, M., Hodgson, J., Brogt, E., Tadhunter, C. N., Mahony, E., Oosterloo, T. A. 2016, A&A, 596, 19
Emonts, B. H. C., Piqueras-López, J., Colina, L., Arribas, S., Villar-Martín, M., Pereira-Santaella, M., Garcia-Burillo, S., Alonso-Herrero, A. 2014, A&A, 572, 40
Fabian, A. C. 2012, ARA&A, 50, 455
Faucher-Giguére, C. A., Quataert, E. 2012, MNRAS, 425, 605
Fiore, F., et al. 2017, A&A, in press, arXiv:1702.04507
García-Burillo, S., Combes, F., Schinnerer, E., Boone, F., Hunt, L. K. 2005, A&A, 441, 1011
Gagne, J. P., Crenshaw, D. M., Kraemer, S. B., et al. 2014, ApJ, 792, 72
García-Burillo, S., et al. 2014, A&A, 567, 125
Gelbord, J. M., Mullaney, J. R., Ward, M. J. 2009, MNRAS, 397, 172
Harrison, C. M., Thomson, A. P., Alexander, D. M., Bauer, F. E., Edge, A. C., Hogan, M. T., Mullaney, J. R., Swinbank, A. M. 2015, ApJ, 800, 45
Harrison, C. M., Alexander, D. M., Mullaney, J. R., Swinbank, A. M. 2014, MNRAS, 441, 3306
Heckman, T. M., González-Delgado, R., Leitherer, C., Meurer, G. R., Krolik, J., Wilson, A. S., Koratkar, A., Kinney, A. 1997, ApJ, 482, 114
Helfer, T. T., Thornley, M. D., Regan, M. W., Wong, T., Sheth, K., Vogel, S. N., Blitz, L., Bock, D. C.-J. 2003, ApJS, 145, 259
Hicks, E. K. S., Davies, R. I., Maciejewski, W., Emsellem, E., Malkan, M. A., Dumas, G., Müller-Sánchez, F., Rivers, A. 2013, ApJ, 768, 107
Hollenbach D., McKee C. F. 1989, ApJ, 342, 306
Hummer, D. G., Storey, P. J. 1987, MNRAS, 224, 801
Humphrey, A., et al. 2010, MNRAS, 408, L1
Husemann, B., Scharwächter, J., Bennert, V. N., Mainieri, V., Woo, J.-H., Kakkad, D. 2016, A&A, 594, A44
Karouzos, M., Woo, J.-H., Bae, H.-J. 2016, ApJ, 819, 148
Keel, W. C., et al. 2016, ApJ, 835, 256
Keel, W. C., et al. 2015, AJ, 149, 155
Keel, W. C., et al. 2012, MNRAS, 420, 878
Korista, K. T., Ferland, G. J. 1989, ApJ, 343, 678
Lal, D. V., Ho, L. C. 2010, AJ, 139, 1089
Landt, H., Ward, M. J., Steenbrugge, K. C., Ferland, G. J. 2015, MNRAS, 449, 3795
Lapi, A., Cavaliere, A., Menci, N. 2005, ApJ, 619, 60
Liu, G., Zakamska, N., Greene, J. E., Nesvadba, N. P. H., Liu, X. 2013, MNRAS, 430, 2327
Maloney P. R., Hollenbach D. J., Tielens A. G. G. M. 1996, ApJ, 466, 561
Mazzalay X., et al. 2013, MNRAS, 428, 2389
Menci, N., Fiore, F., Puccetti, S., Cavaliere, A. 2008, ApJ, 686, 219
Mouri, H. 1994, ApJ, 427, 777
Mullaney J. R., Alexander, D. M., Fine, S., Goulding, A. D., Harrison, C. M., Hickox, R. C. 2013, MNRAS, 433, 622
Mullaney J. R., Ward M. J., Done, C., Ferland, G. J., Schurch, N. 2009, MNRAS, 394, L16
Mullaney J. R., Ward M. J., 2008, MNRAS, 385, 53
Müller-Sánchez, F., Comerford, J., Stern, D., Harrison, F. A. 2016, ApJ, 830, 50
Müller-Sánchez, F., Prieto, M. A., Hicks, E. K. S., Vives-Arias, H., Davies, R. I., Malkan, M., Tacconi, L. J., Genzel, R. 2011, ApJ, 739, 69
Müller-Sánchez, F., Davies, R. I., Eisenhauer, F., Tacconi, L. J., Genzel, R., Sternberg, A. 2006, A&A, 454, 481
Penston M. V., Fosbury R. A. E., Boksenberg A., Ward M. J., Wilson A. S., 1984, MNRAS, 208, 347
Piqueras López, J., Colina, L., Arribas, S., Pereira-Santaella, M. Alonso-Herrero, A., 2016, A&A, 590, A67
Piqueras López, J., Colina, L., Arribas, S., Alonso-Herrero, A., Bedregal, A. G. 2012, A&A, 546, A64
Ramos Almeida, C., Pérez García, A. M., Acosta-Pulido, J. A. 2009, ApJ, 694, 1379
Reunanen J., Kotilainen J. K., Prieto M. A. 2002, MNRAS, 331, 154
Reyes, R., et al. 2008, AJ, 136, 2373
Riffel, R., Rodríguez-Ardila, A., Pastoriza, M. G. 2006, A&A, 457, 61
Rodríguez-Ardila, A., Prieto, M. A., Portilla, J. G., Tejeiro, J. M. 2011, ApJ, 743, 100
Rodríguez-Ardila, A., Prieto, M. A., Viegas, S., Gruenwald,

R. 2006, ApJ, 653, 1098
Rodríguez-Ardila, A., Mazzalay, X. 2006, MNRAS, 367, L57
Rose, M., Tadhunter, C. N., Holt, J., Ramos Almeida, C., Littlefair, S. 2011, MNRAS, 414, 3360
Tadhunter, C., Morganti, R., Rose, M., Oonk, J. B. R., Oosterloo, T. 2014, Nature, 511, 440
Tadhunter, C., Shaw, M., Clark, N., Morganti, R. 1994, A&A, 288, L21
Villar-Martín, Arribas, S., Emonts, B., Humphrey, A., Tadhunter, C., Bessiere, P., Cabrera Lavers, A., Ramos Almeida, C. 2016, MNRAS, 460, 130
Villar Martín, M., Bellocchi, E., Stern, J., Ramos Almeida, C., Tadhunter, C., González Delgado, R. 2015, MNRAS, 454, 439
Villar-Martín, M., et al. 2013, MNRAS, 434, 978
Villar-Martín, M., Emonts, B., Humphrey, A., Cabrera Lavers, A., Binette, L. 2014, MNRAS, 440, 3202
Villar-Martín, M., Humphrey, A., González Delgado, R., Colina, L., Arribas, S. 2011, MNRAS, 418, 2032
Villar-Martín, M., Tadhunter, C., Morganti, R., Axon, D., Koekemoer, A. 1999, MNRAS, 307, 24
Zakamska, N. L., Greene, J. E. 2014, MNRAS, 442, 784
Zubovas, K., King, A. 2012, ApJ, 745, L34